

TRANSITION FROM YOUNG TO MIDDLE-AGED SUPERNOVA REMNANTS: THERMAL AND NONTHERMAL ASPECTS OF THE SNR N132D

AYA BAMBA^{1,2}, YUTAKA OHIRA³, RYO YAMAZAKI³, MAKOTO SAWADA^{3,4,5}, YUKIKATSU TERADA⁶, KATSUJI KOYAMA^{7,8}, ERIC D. MILLER⁹, HIROYA YAMAGUCHI^{10,11}, SATORU KATSUDA^{12,6}, MASAYOSHI NOBUKAWA¹³, KUMIKO K. NOBUKAWA¹⁴

ABSTRACT

Supernova remnants (SNRs) are the primary candidate of Galactic cosmic-ray accelerators. It is still an open issue when and how young SNRs, which typically exhibit strong synchrotron X-rays and GeV and TeV gamma-rays, undergo the state transition to middle-aged SNRs dominated by thermal X-rays and GeV gamma-rays. The SNR N132D in the Large Magellanic Cloud is an ideal target to study such a transition, exhibiting bright X-rays and gamma-rays, and with the expected age of ~ 2500 yrs. In this paper we present results of *NuSTAR* and *Suzaku* spectroscopy. We reveal that N132D has a nearly equilibrium plasma with a temperature of > 5 keV or a recombining plasma with a lower temperature (~ 1.5 keV) and a recombining timescale ($n_{\text{e}t}$) of $8.8 (7.0\text{--}10.0) \times 10^{12} \text{ cm}^{-3}\text{s}$. Together with the center filled morphology observed in the iron K line image, our results suggest that N132D is now at transition stage from a young SNR to middle-aged. We have constrained the tight upper-limit of nonthermal X-rays. Bright gamma-rays compared to faint nonthermal X-rays suggest that the gamma-rays are hadronic in origin. The spectral energy distribution from radio to gamma-rays shows a proton cut-off energy of ~ 30 TeV. These facts confirm that N132D is in the transition from young to middle-aged SNR. The large thermal energy of $> 10^{51}$ erg and accelerated proton energy of $\sim 10^{50}$ erg suggest the supernova explosion might have been very energetic.

Subject headings: ISM: individual (N132D) — cosmic rays — supernova remnants — X-rays: ISM — gamma-rays: ISM

1. INTRODUCTION

Supernova remnants (SNRs) play crucial roles in physical processes at the universe: e.g., they work as energy and heavy element suppliers, and accelerate cosmic rays at their shocks. They evolve in a rather short time scale in the interstellar medium. Young SNRs expand with high shock velocity and emit strong thermal and nonthermal X-rays from their shells. Synchrotron X-rays are excellent tools to detect accelerated electrons (Koyama et al. 1995), in addition to understand one of the key parameters, the magnetic field, from its small-scale and sometimes time-variable structures (Vink

& Laming 2003; Bamba et al. 2005; Uchiyama et al. 2007), and thus to resolve the origin of gamma-rays (Aharonian et al. 2007, for example).

On the other hand, middle-aged SNRs are fainter in both thermal and nonthermal emission, and as a result, the study has developed rather recently. *Fermi*/LAT has detected significant soft gamma-rays from many old SNRs (The Fermi-LAT Collaboration 2015), implying that old SNRs still keep high energy particles into the space. However, the detailed nature of these nonthermal emission is still poorly understood, since no synchrotron X-rays have been detected from middle-aged SNRs to date. no synchrotron X-ray emission has been reported so far from middle-aged SNRs.

It is also noteworthy that most of the GeV-bright SNRs contain recombining plasma (e.g., Yamaguchi et al. 2009), implying that the plasma experienced rapid cooling during the SNR evolution. Such a plasma emits strong radiative recombination continuum and produces hard tails in the X-ray spectra. Resolving this component will help to understand the environment of particle acceleration sites.

N132D is the X-ray/gamma-ray brightest SNR in the Large Magellanic Cloud (LMC) (Sutherland & Dopita 1995). It has a ~ 14 pc ellipsoidal shell expanding with the average speed of 1650 km s^{-1} (Morse et al. 1995). The SNR age is about 2500 yrs (Vogt & Dopita 2011). *Chandra* and *XMM-Newton* spectra showed multi-temperature thermal emission with strong emission lines from O to Fe (Behar et al. 2001; Borkowski et al. 2007). Williams et al. (2006) reported a high dust density of $> 15 \text{ cm}^{-3}$, a conclusion supported by the detection of a CO cloud with the mass of $\sim 2 \times 10^5 M_{\odot}$ in the south of the SNR (Banas et al. 1997; Sano et al. 2015). The southern part shows an enhanced thermal X-ray emission with circular shape, which supports the presence of dense ambient medium, whereas the northern part has blown-out shape, implying low-density interstellar medium in this direction. Recently, GeV and Very high energy (VHE) gamma-

¹ Department of Physics, Graduate School of Science, The University of Tokyo, 7-3-1 Hongo, Bunkyo-ku, Tokyo 113-0033, Japan

² Research Center for the Early Universe, School of Science, The University of Tokyo, 7-3-1 Hongo, Bunkyo-ku, Tokyo 113-0033, Japan

³ Department of Physics and Mathematics, Aoyama Gakuin University 5-10-1 Fuchinobe Chuo-ku, Sagami-hara, Kanagawa 252-5258, Japan

⁴ X-ray Astrophysics Laboratory, NASA Goddard Space Flight Center, Greenbelt, MD 20771, USA

⁵ Department of Physics, University of Maryland Baltimore County, 1000 Hilltop Circle, Baltimore, MD 21250, USA

⁶ Department of Physics, Science, Saitama University, Sakura, Saitama 338-8570, Japan

⁷ Department of Physics, Graduate School of Science, Kyoto University, Kitashirakawa-oiwake-cho, Sakyo-ku, Kyoto 606-8502, Japan

⁸ Department of Earth and Space Science, Graduate School of Science, Osaka University, 1-1 Machikaneyama-cho, Toyonaka, Osaka 560-0043, Japan

⁹ Kavli Institute for Astrophysics & Space Research, Massachusetts Institute of Technology, 77 Massachusetts Avenue, Cambridge, MA 02139, USA

¹⁰ NASA Goddard Space Flight Center, Code 662, Greenbelt, MD 20771, USA

¹¹ Department of Astronomy, University of Maryland, College Park, MD 20742, USA

¹² Department of Physics, Faculty of Science & Engineering, Chuo University, 1-13-27 Kasuga, Bunkyo, Tokyo 112-8551, Japan

¹³ (Department of Teacher Training and School Education, Nara University of Education, Takabatake-cho, Nara, 640-8528, Japan

¹⁴ Department of Physics, Nara Women's University, Kitaouyanishimachi, Nara 630-8506, Japan

rays have been detected from N132D by *Fermi* and H.E.S.S. (The Fermi-LAT Collaboration 2015; H.E.S.S. Collaboration et al. 2015). The gamma-ray spectrum is very hard like other young SNRs such as Cas A and RX J1713–3946 (Abdo et al. 2010a, 2011). Surprisingly, the measured luminosity in the 1–100 GeV band, $\sim 10^{36}$ erg s⁻¹ at 48 kpc (Macri et al. 2006), is two orders of magnitude higher than those of typical young SNRs. Actually this is the highest luminosity among all known GeV SNRs (Acero et al. 2016). Such a feature in the gamma-ray band implies that N132D is an energetic cosmic-ray supplier. Furthermore, it is difficult to make such bright gamma-rays with leptonic models, suggesting that gamma-rays are hadronic in origin. Interestingly, we have no report of a synchrotron X-ray detection from this source, probably because the soft X-ray spectrum is dominated by the luminous, high-temperature thermal X-rays up to Fe-K line band (Behar et al. 2001; Borkowski et al. 2007; Yamaguchi et al. 2014). We need sensitive observations in the hard X-ray band above 10 keV, where thermal emission becomes much fainter. *NuSTAR* is an ideal observatory for such a study with its hard X-ray imaging system (Harrison et al. 2013). *Suzaku* also has a large effective area, and low, stable background in the hard X-ray band, suitable for the nonthermal emission search (Mitsuda et al. 2007).

In this paper, we present the first results of the hard X-ray observation of N132D with *NuSTAR* and *Suzaku*. §2 and §3 describe the observation details and the analysis results, respectively. In §4 we discuss the condition of particle acceleration on N132D together with radio, infrared, GeV and VHE gamma-ray results. In this work, data reduction and analysis were performed with HEADAS version 6.20 and XSPEC version 12.9.1. For the spectral analysis, atomic data base (ATOMDB) version 3.0.8 and the *nei* version (NEIVERS) 3.0.7 were used. Throughout the paper, we use 90% error bars and confidence intervals.

2. OBSERVATIONS AND DATA REDUCTION

2.1. *NuSTAR*

N132D has been observed by the pixelated CdZnTe focal plane modules, FPMA and FPMB, onboard *NuSTAR* with a single pointing on 2015 Dec. 10–11. The data were reprocessed with the calibration data base (ver.20151008). The cleaned events were extracted with the standard screening criteria, except for the criteria for the passage of the South Atlantic Anomaly (SAA). Since our target is faint in the hard band, and the background count rate slightly elevated around the SAA, we started the analysis with data filtered with the parameters SAAMODE=STRICT and TENTACLE=yes. The total exposure is 62.3 ks, which is 90% of the nominal screening case. The observation log is shown in Table 1.

2.2. *Suzaku*

N132D has been observed by *Suzaku* several times for calibration purposes. We selected all data except for those taken in *Suzaku* initial operation. The details of observations are shown in Table 1. *Suzaku* has several kinds of detectors, four X-ray Imaging Spectrometers (XIS0–XIS3; Koyama et al. (2007a)) with each at the focus of an X-Ray Telescope (XRT; Serlemitsos et al. (2007)), and a separate Hard X-ray Detector (HXD; Takahashi et al. (2007)). We concentrate on the analysis of XIS, since *NuSTAR* has much better sensitivity than HXD. We have checked the HXD data and found no significant signal. Only three XISs operated in all of these observations. XIS1 is a back-illuminated (BI) CCD, whereas the

others are front-illuminated (FI). The XISs were operated in normal full-frame clocking mode with spaced-row charge injection (Nakajima et al. 2008; Uchiyama et al. 2009). The data was reprocessed with the calibration database version 2016-02-14 for XIS and 2011-06-30 for XRT. We applied the standard screening criteria to create the cleaned event list. The total exposure is 240.3 ks. The observation log is shown in Table 1.

3. RESULTS

3.1. *NuSTAR*

3.1.1. *Images*

Figure 1 shows *NuSTAR* 3–10 keV (a), 10–15 keV (b), and 15–40 keV (c) images, where both FPMA and FPMB were used. We can see clear enhancement on the N132D region below 15 keV, whereas it is not clear above 15 keV. The remnant has a size of $\sim 0.7 \times 1.0$ arcmin², which is smaller than the point spread function of *NuSTAR* and we could not resolve the extension or structure.

We also found stray light from LMC X-4 in both detectors and that from LMC X-2 in FPMB (see Figure 1). Another nearby high mass X-ray binary, XMMU J054134.7–682550, can produce stray light since it sometimes show the flaring (Liu et al. 2005; Palmer et al. 2007). We have checked *Swift*/BAT observations (Krimm et al. 2013), and found that it was in the steady state with the flux of only ~ 1 mCrab, and that it did not show any flare during our observation. We thus ignore the stray light effect by XMMU J054134.7–682550.

3.1.2. *Spectra*

The source photons were extracted from a 1.4 arcmin-radius region centered on N132D, whereas we selected the background region free from other sources and stray lights, as shown in Figure 1. The response files are produced with the *nuproducts* command under the point source assumption.

Figure 2 shows the background-subtracted spectra of *NuSTAR* FPMA and FPMB. One can see emission-like structures around 6.5 and 7.9 keV. The former is reported as a K α emission line from He-like Fe (Borkowski et al. 2007; Yamaguchi et al. 2014), whereas there is no report on the latter. We fitted the spectra with a bremsstrahlung plus two Gaussian components. The *c*-statistic (Cash 1979) was used throughout this paper. The background spectra were fitted simultaneously in XSPEC, whereas background-subtracted spectra were used for the spectral plot¹⁵. The best-fit models and parameters are shown in Figure 2 and Table 2. From the line center energies, we identified the 6.66 keV line as He-like Fe K α , and 7.9 keV line as He-like Ni K α or He-like Fe K β . One can also see the residuals above 10 keV, which can be nonthermal hard tail or higher-temperature component. The flux above 10 keV is $2.4 (2.0\text{--}2.8) \times 10^{-14}$ erg cm⁻²s⁻¹.

3.2. *Suzaku*

3.2.1. *Images*

Figure 3 shows the *Suzaku* XIS3 5–10 keV image. We used only XIS3 since the part of XIS0 is not available and XIS1 has low efficiency and high background in this energy band. One can see a point-like source in the center of the field of view.

3.2.2. *Spectra*

¹⁵ see <https://heasarc.gsfc.nasa.gov/docs/xanadu/xspec/manual/node293.html>

We extracted source photons from a circular region with a radius of 2 arcmin as shown in Figure 3. The background spectra mainly contain the Non X-ray Background (NXB) and Cosmic X-ray Background (CXB) above 5 keV. Other background components such as local hot bubble (Yoshino et al. 2009) and LMC diffuse plasma (Points et al. 2001) have a temperature of less than 1 keV, which is negligible in our band. The NXB is generated by `xisnxbgen` (Tawa et al. 2008) for 7 arcmin radius region (see Figure 3) and adjusted with the 11–14 keV count rate, where we expect neither source nor CXB emission (Sekiya et al. 2016). We reproduced the CXB emission by the power-law model with the photon index of 1.4 and the surface brightness in the 2–10 keV band of $5.4 \times 10^{-15} \text{ erg s}^{-1} \text{ cm}^{-2} \text{ arcmin}^{-2}$ (Ueda et al. 1999). Since our target is point-like whereas the CXB is uniformly distributed, we simulated the CXB spectrum with the assumption of uniform distribution within 1.4 arcmin radius region and fit it with the point source `arf`, and used the best-fit parameters in N132D spectral fitting.

Figure 4 shows the NXB-subtracted XIS spectrum above 5 keV. One can see clear emission lines, similar to the *NuSTAR* results. We fit the spectrum with bremsstrahlung plus 2 narrow gaussian model. The fit returned `cstat/d.o.f.` of 167.5/111 with positive residuals around 6.9 keV, which could not seen in the *NuSTAR* spectra maybe due to the lack of statistics and energy resolution. We added one more narrow gaussian to represent this structure, which improved the `cstat/d.o.f.` to 145.4/109. The line center energy agrees with the Fe Ly α emission line, and this is the first detection of this line from N132D. We still have small positive residuals in the high energy end, which is consistent with the *NuSTAR* data. Table 3 shows the best-fit parameters.

3.3. Combined spectral Analysis

In the previous subsection, we reported the first detection of Fe Ly α emission from N132D, indicating that a substantial fraction of Fe atoms in this SNR is highly ionized. Keeping this in mind, we here constrain thermal parameters with *NuSTAR* and *Suzaku* combined spectral analysis. We start the fitting with 5–15 keV band. We first introduce a `vapec` model, a plasma in ionization equilibrium. We used the photoionization cross-section table by Balucinska-Church & McCammon (1992). The abundances of Fe and Ni were treated as a common free parameter, whereas those of the other elements were fixed to the solar values (Anders & Grevesse 1989). The best fit was obtained with an electron temperature of 2.31 (2.23–2.39) keV and `cstat/d.o.f.` of 195.2/142, leaving positive residuals around 6.9 keV due to the Fe Ly α line detected in the *Suzaku* spectrum. This implies that the average charge balance is higher than the temperature predicted by the ionization equilibrium model. We thus added a second `vapec` component and found that the fit was improved significantly (`cstat/d.o.f.` = 134.6/140), with kT of 1.1 (0.9–1.3) keV and 5.0 (4.5–6.3) keV. A higher charge balance is also achieved when the plasma is over-ionized. We thus replaced the second `vapec` model with a `vrnei` model having a higher initial temperature to represent a recombining plasma. This model also improved the fitting with `cstat/d.o.f.` of 173.4/140. We still have positive residuals in higher energy band, which can be nonthermal emission from accelerated electrons. We thus added a power-law component. The photon index is fixed to 2.4, same to the gamma-ray emission. The fitting was improved to `cstat/d.o.f.` of 155.8/139.

In the next step of adding the power law component, we

extended the fitting range to 2–15 keV band to check the plasma condition of these higher temperature components. In the energy band below ~ 3 keV, we already know that there is at least one lower temperature component (Borkowski et al. 2007), thus we added one more `vapec` component with lower temperature. Hereafter, we call “model (a)” for the three `apec` plasma model and “model (b)” for the two `apec` plus a `vrnei` plasma model. We fixed the abundances of the low temperature compoet to the LMC abundance (Russell & Dopita 1992), but the best-fit model has significant residuals on Si and S lines. We thus left the abundances of Si and S for the low temperature component free. The abundances of Si and S, and Fe and Ni of middle temperature component were treated as common free parameters, whereas the other elements were assumed solar abundance. We made fine tuning of XIS gain offset and treated cross-normalization of each detector as free parameters. We ignored the Galactic absorption column to the direction of N132D ($1.6 \times 10^{21} \text{ cm}^{-2}$; Kalberla et al. 2005), since it increases flux only 3% in the 2–10 keV, and 0.3% in the 6–7 keV band, which we are especially interested in for the Fe K line. Both models well reproduce the observed spectrum. The gain offset obtained is 3–5 eV for FI and 9 eV for BI, which is roughly within the range of the XIS gain uncertainty. We find small residuals around 6.4 keV. We attribute this feature to fluorescence emission from neutral Fe, and thus added a narrow gaussian with fixed center energy of 6.4 keV. The fitting was improved, with a significance level of this emission component of 0.7σ for model (a) and 3.8σ for model (b). Finally, we estimate flux (or its upper limit) of nonthermal X-rays by adding a power-law component. We fixed the photon index to be 2.4, same value as that in the gamma-ray band. The fitting was improved with 3.3σ detection power-law component for model (a) and 30σ detection for model (b). The best-fit models and parameters are shown in Figure 5 and Table 4, respectively. We also tried the fittings with the free photon index, but we could not determine the photon index well (>1.8 for model (a) and 1.2–3.0 for model (b) for the single parameter errors). Both models have similar `cstats/d.o.f` values and leave no large structure in the residuals. Therefore, we cannot conclude which model better represents the observed X-ray spectrum from the statistical point of view. In order to determine the parameters of both thermal and non-thermal component, we need further observations with excellent energy resolution such as Hitomi (Hitomi Collaboration et al. 2017).

For the further check of the origin of hard X-rays, we compared a iron K line image and 10–15 keV band image of *NuSTAR*. The iron line band was defined as 6.0–7.2 keV from Figure 2. The band image also contains the continuum emission. We estimated the contamination of the continuum component with the spectral fitting result shown in Table 2, and subtracted. Figure 6 shows the iron K line (blue) and 10–15 keV band (green) images. Both show no enhancement on the outer-edge regions shown in the *Chandra* image (white contour). Further investigation with good statistics and spatial resolution is needed.

3.4. Comments on pile-up effect on Suzaku spectra

N132D is very bright in X-rays, and we should be careful about pile-up effect especially for the *Suzaku* data set, which can mimic the hard tail in the spectra. We thus investigate the pile-up effect in *Suzaku* spectra to judge whether the power-law component we detected is the result of pile-up or not. As the first step, we have checked the pile-up fraction with the

fool pileest, and found that the fraction is smaller than 4% for FI and 6% for BI. This is the average value for the all energy band, whereas our special interest is in harder energy band. Thus as the next step we simulated the piled-up and non-piled up spectra and compared them. It is found that the upper-limit of the ratio of flux coming from piled-up events to the total is $\sim 10\%$ in 8–10 keV band. The flux ratio of the power-law component to the total in the 8–10 keV band is 10% for model (a) and 20% for model (b). The former is in the range of expected pile-up, whereas the latter is still larger than the expected pile-up ratio. Since we cannot judge which model is better, We thus treat the larger end of the error region of the power-law flux as the upper-limit with systematic errors.

4. DISCUSSION

4.1. Thermal emission

Thanks to the large effective area of *NuSTAR*, and low and stable background of *Suzaku* XIS above 5 keV, we detected significant Fe Ly α emission line for the first time. This suggests the existence of either a very high temperature (model (a)) or over-ionized (recombining) component (model (b)). Although these models cannot be distinguished from statistical point of view, the temperature required in model (a) is unusually high as a middle-aged SNR. Moreover, this model requires high abundances of Si and S in the low temperature component, inconsistent to the previous observations. We thus assume model (b) to be a reasonable interpretation for the high-temperature plasma in N132D and discuss its origin hereafter.

SNRs with recombining plasma have several characteristics. They are usually associated with GeV gamma-ray emission coming from molecular clouds. They also exhibit mixed-morphology (MM) shape (radio shell plus center-filled thermal X-rays; Rho & Petre 1998) (c.f., Yamaguchi et al. 2009). However, N132D does not have a typical MM shape but rather a shell-like morphology in the soft X-ray band (Borkowski et al. 2007). The iron K line image, on the other hand, shows a center-filled morphology (Behar et al. 2001; Plucinsky et al. 2015). These facts imply that the low temperature component mainly studied in previous works makes the shell-like structure, whereas the recombining component remains in the center of the remnant. These results may indicate again that N132D is in the transition stage from shell-like young SNRs to old ones with MM morphology; during the transition, the center-filled emission appears first, and after that the low temperature emission from the shell will disappears to make the MM morphology. In summary, it is expected that N132D is in transition phase.

In order to derive the density and thermal energy, the uniform density sphere with the radius of 30 arcsec or 7 pc at 48 kpc was assumed (Macri et al. 2006). We derived the density from the emission measure $\sim 3 \text{ cm}^{-2}$. The thermal electron energy of the recombining component, $3n_e kT$ times volume, is estimated to be $\sim 9 \times 10^{50}$ erg. Combining those of lower temperature components (Behar et al. 2001; Borkowski et al. 2007), the total thermal energy exceed $\sim 10^{51}$ erg. Moreover, the kinetic energy should be dominant when SNRs are young, thus the total energy exceeds 10^{51} erg even more. This result implies that the progenitor explosion of N132D might be more energetic than usual supernovae.

4.2. Nonthermal emission

N132D is the brightest SNR in the gamma-ray band (The Fermi-LAT Collaboration 2015; H.E.S.S. Collaboration et al. 2015). We estimated an upper-limit on the nonthermal X-ray flux of $7.3 \times 10^{-13} \text{ ergs s}^{-1} \text{ cm}^{-2}$ or $2.0 \times 10^{35} \text{ erg s}^{-1}$ in the 2–10 keV band. This is fainter than the younger samples, Cas A (Helder & Vink 2008). Nakamura et al. (2012) suggests that the nonthermal X-ray luminosity becomes fainter when SNRs get older, thus our faint nonthermal X-rays in N132D is consistent with the older age. The primary nonthermal emission mechanism in the X-ray band is synchrotron from accelerated electrons, whereas GeV and VHE gamma-rays have leptonic origin via inverse Compton and/or hadronic origin via π^0 decay, respectively. The ratio between TeV gamma-ray flux in 1–10 TeV (F_{TeV}) and synchrotron X-ray flux in 2–10 keV (F_X), F_{TeV}/F_X , is useful to resolve these two possibilities (Yamazaki et al. 2006; Matsumoto et al. 2007; Bamba et al. 2007). In our case, F_{TeV}/F_X is larger than 7, which is much larger than young SNRs with strong synchrotron X-ray filaments (Yamazaki et al. 2006). This result implies that gamma-rays from N132D have a hadronic origin. This agrees with the observational fact that the GeV gamma-ray luminosity is $\sim 10^{36} \text{ erg s}^{-1}$, which is very difficult to reproduce with the inverse compton scattering of the cosmic microwave background ($\sim 10^{35} \text{ erg s}^{-1}$; Acero et al. 2016; Bamba et al. 2016). A more detailed discussion will be found in the following.

Figure 7 shows the broad-band spectral energy distribution (SED) of N132D for a more quantitative study. 3.5 cm and 6 cm data were taken from Dickel & Milne (1995), whereas we used *PLANCK* data points at 100 GHz (Planck Collaboration et al. 2014). Planck Collaboration et al. (2014) used 2.6 arcmin radius region for the source spectra, which includes surrounding molecular clouds. We thus used this data point as an upper-limit. Our analysis concentrates on the hard X-rays, whereas *ASCA* shows the upper-limit of nonthermal emission in the 0.5–5 keV band with the assumption of $\Gamma = 2$ (Hughes et al. 1998). *Fermi* and H.E.S.S. data points were also used (The Fermi-LAT Collaboration 2015; H.E.S.S. Collaboration et al. 2015).

The solid lines in the left panel of Figure 7 represent a pure leptonic model to reproduce the data points. We assumed the photon field of inverse compton emission in the same way of H.E.S.S. Collaboration et al. (2015), the infrared emission from dust in and around the SNR. This model requires the magnetic field of $\leq 20 \mu\text{G}$, the cut-off energy for electron of 7 TeV, and the total amount of energy of electrons (U_e) of 2.5×10^{49} erg. The derived U_e is very large and unrealistic in a typical SNR, since we should also consider the energy of accelerated protons, which should be comparable or larger than that of electrons (Slane et al. 2016). The total electron energy does not change even if we assume different spatial distribution for electrons and protons. These results suggest that the emission cannot have a pure leptonic origin, but instead must have a hadronic one. This result is mainly from bright GeV gamma-rays and faint synchrotron X-rays, which require a small magnetic field and as a result large U_e .

The right panel of Figure 7 represents the leptonic + hadronic model fit to the gamma-ray data. We estimated the maximum energy of accelerated proton E_{max} first from GeV–VHE gamma-ray spectrum, and determined the magnetic field and the amount of electrons with the assumption that electrons and protons have the same maximum energy. We then estimated the inverse compton emission from accelerated electrons and the same infrared photon field to that in our pure leptonic model analysis (H.E.S.S. Collaboration et al. 2015).

When we fix the proton spectral index to be 2.0 and a total proton energy of 10^{50} erg, we estimated the number density of 80 cm^{-3} for the pre-shock interstellar gas and E_{max} of 30 TeV. Assuming electron cut-off energy is same to E_{max} , we derived U_e of $\leq 10^{48}$ erg and magnetic field of $\leq 13 \mu\text{G}$.

The presence of a molecular cloud around the SNR supports the large number density of ambient matter. The best-fit proton energy is $\sim 10\%$ of the typical explosion energy. Note that the derived energy is only for those emitting gamma-rays, so that more energy is required if there are accelerated protons which do not emit gamma-rays. These facts suggest that N132D is a very energetic cosmic ray accelerator. This result can be connected to our results from thermal aspects, that the progenitor explosion was more energetic than conventional supernovae.

Many old SNRs with gamma-rays are now identified as emitting from accelerated protons with the maximum energy of ~ 10 GeV (for example, W44 (Abdo et al. 2010b), W28 (Abdo et al. 2010c)). On the other hand, the gamma-ray spectrum of N132D is harder than the spectra from such old SNRs, extending up to \sim TeV range. Figure 8 shows the SED of RX J1713–3946 as typical young SNR case (H. E. S. S. Collaboration et al. 2016), W44 as a typical middle-aged (Ackermann et al. 2013), and N132D. It is widely agreed that the gamma-ray emission from W44 is hadronic origin, whereas in the case of RX J1713–3946, there is still debate about whether it is leptonic (Ellison et al. 2010; Ohira & Yamazaki 2017) or hadronic (Inoue et al. 2012; Gabici & Aharonian 2014; Yamazaki et al. 2009). One can see that the cut-off energy of the gamma-ray spectrum of N132D is between those of W44 and RX J1713–3946. Actually, the maximum energy of accelerated protons in N132D (30 TeV) is between that for RX J1713.7–3946 (> 100 TeV; Aharonian et al. 2007) and W44 (7–9 GeV; Abdo et al. 2010b). Our comparison implies that N132D is in a transition phase from young to old, also in the context of particle acceleration.

Protons are accelerated to high energies when SNRs are young, and start escaping when SNRs get older or interact with molecular clouds (Ptuskin & Zirakashvili 2005; Ohira et al. 2010, 2012) and emit gamma-rays (Gabici et al. 2009; Ohira et al. 2011). Since N132D is in the transition phase, the remnant has already accelerated protons to very high energies, and still produces them at a rate higher than it loses them. This may explain the exceptionally bright gamma-ray emission from N132D.

4.3. Comments on the neutral iron K line

We detected possible signal of neutral iron K line from N132D. The luminosity of the line is $\sim 1.9 \times 10^{33}$ erg s^{-1} assuming a distance of 48 kpc (Macri et al. 2006).

Neutral iron K line from SNRs is rather peculiar, since the SNR plasma is highly ionized. RCW 86 has strong neutral iron K emission (Bamba et al. 2000), which is from plasma with very low ionization time scale (Yamaguchi et al. 2008). The line luminosity is 3.2×10^{32} erg s^{-1} (Ueno et al. 2007) with the distance of 2.3 kpc (Sollerman et al. 2003), which is similar to that in our case. On the other hand, this low ionization plasma in RCW 86 has been heated very recently via the interaction with the cavity wall (Broersen et al. 2014), which is not our case since the main plasma in N132D is over-ionized.

Other samples with the neutral iron K line are 3C391 (Sato et al. 2014) and Kes 79 (Sato et al. 2016a). The former has

the line luminosity of $\sim 1.5 \times 10^{32}$ erg s^{-1} (Sato 2016b) at 8 kpc (Reynolds & Moffett 1993), whereas the latter has the line luminosity of 2.8×10^{32} erg s^{-1} at 7.5 kpc (Giacani et al. 2009), slightly smaller but comparable within the large error region of our case. Sato et al. (2016a) claims the possibility that the line from Kes 79 is due to K-shell ionization of neutral iron by the interaction of low-energy cosmic-ray protons with the surrounding molecular cloud, since the peak position of the line emission coincides with the molecular cloud (Giacani et al. 2009), together with the detection of GeV gamma-rays (Auchettl et al. 2014). Similar discussion can be done for 3C391, together with OH masers (Frail et al. 1996) and GeV emission (Castro & Slane 2010). W44 is also similar to this sample with the possible detection of neutral iron K line ($7.0 \pm 5.0 \times 10^{-6}$ ph $\text{cm}^{-2}\text{s}^{-1}$; Sato 2016b) and GeV gamma-ray emission (Acero et al. 2016). If these lines are due to low-energy cosmic-ray protons, the luminosities of neutral iron K line and GeV gamma-ray may have a positive correlation, since the former is roughly proportional to the number of low-energy cosmic-ray protons in the MeV range and target mass (e.g., Valinia et al. 2000; Dogiel et al. 2011; Nobukawa et al. 2015) whereas the latter to the number of GeV protons and target mass. Figure 9 shows the relation between neutral iron K line and 0.1–100 GeV gamma-ray luminosities of these SNRs. Although the sample number is too small and the error is large, the tendency is consistent with our scenario. It can be the first clue of the proton acceleration in the MeV range in SNRs. In order to study this issue further, we need more X-ray observations with good energy and spatial resolution and better statistics.

5. CONCLUSIONS

We have performed X-ray spectroscopy of the SNR N132D in the LMC, using *NuSTAR* and *Suzaku* deep observations. Thanks to the large effective area and low, stable background, we discover that a very high temperature plasma or recombining plasma with $nt \sim 8.8 \times 10^{11}$ cm^{-3}s . Together with the morphology of the iron K emission, we conclude that N132D is in the transition phase from young shell-like SNR with ionizing plasma to middle-aged mixed morphology SNR with recombining plasma. The total thermal energy of $> 10^{51}$ erg shows the progenitor explosion of N132D can be very energetic. We have made the tight upper-limit of nonthermal X-rays. The spectral energy distribution from radio to VHE gamma-rays shows us that the total energy of accelerated protons is very energetic, implying that N132D is a very efficient proton accelerator. The cut-off energy in the gamma-ray band also shows that N132D is in a transition stage from young to middle-aged.

We thank the anonymous referee for the fruitful comments. We thank The TeGeV Catalogue at ASDC (v2) (<http://tools.asdc.asi.it/catalogSearch.jsp>) to make the SED. This research has made use of NASA's Astrophysics Data System Bibliographic Services, and the SIMBAD database, operated at CDS, Strasbourg, France. This work is supported in part by Grant-in-Aid for Scientific Research of the Japanese Ministry of Education, Culture, Sports, Science and Technology (MEXT) of Japan, No. 22684012 and 15K051017 (A. B.), 16K17702 (Y. O.), 15K05088 (R. Y.), 15K17657 (M. S.), and 16K17673 (S. K.). E. M. acknowledges support from NASA grant NNX15AC76G.

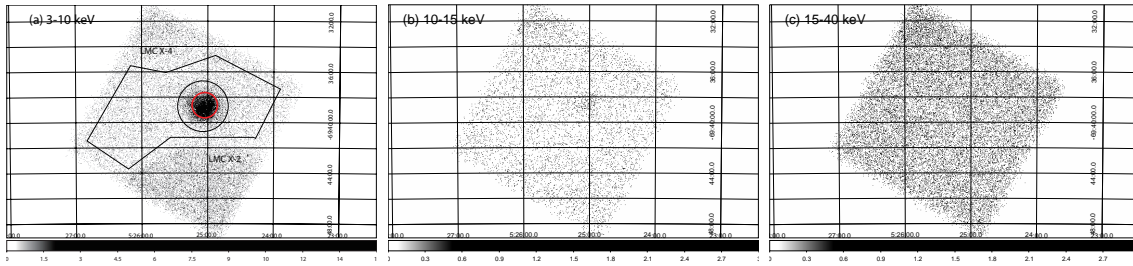


FIG. 1.— The *NuSTAR* FPMA + FPMB images of N132D in (a) 3–10 keV, (b) 10–15 keV, and (c) 15–40 keV band. The images are in the linear scale and the coordinates are in J2000. The stray lights from LMC X-2 and LMC X-4 are also marked. Bold-red and thin-black regions represent source and background regions for the spectral analysis.

REFERENCES

- Abdo, A. A., Ackermann, M., Ajello, M., et al. 2010a, *ApJ*, 710, L92
- Abdo, A. A., Ackermann, M., Ajello, M., et al. 2010b, *Science*, 327, 1103
- Abdo, A. A., Ackermann, M., Ajello, M., et al. 2010c, *ApJ*, 718, 348
- Abdo, A. A., Ackermann, M., Ajello, M., et al. 2011, *ApJ*, 734, 28
- Acero, F., Ackermann, M., Ajello, M., et al. 2016, *ApJS*, 224, 8
- Ackermann, M., Ajello, M., Allafort, A., et al. 2013, *Science*, 339, 807
- Aharonian, F., Akhperjanian, A. G., Bazer-Bachi, A. R., et al. 2007, *A&A*, 464, 235
- Anders, E., & Grevesse, N. 1989, *Geochim. Cosmochim. Acta*, 53, 197
- Auchettl, K., Slane, P., & Castro, D. 2014, *ApJ*, 783, 32
- Balucinska-Church, M., & McCammon, D. 1992, *ApJ*, 400, 699
- Bamba, A., Koyama, K., & Tomida, H. 2000, *PASJ*, 52, 1157
- Bamba, A., Yamazaki, R., Yoshida, T., Terasawa, T., & Koyama, K. 2005, *ApJ*, 621, 793
- Bamba, A., Koyama, K., Hiraga, J. S., et al. 2007, *PASJ*, 59, 209
- Bamba, A., Sawada, M., Nakano, Y., et al. 2016, *PASJ*, 68, S5
- Banas, K. R., Hughes, J. P., Bronfman, L., & Nyman, L.-A. 1997, *ApJ*, 480, 607
- Behar, E., Rasmussen, A. P., Griffiths, R. G., et al. 2001, *A&A*, 365, L242
- Broersen, S., Chiotellis, A., Vink, J., & Bamba, A. 2014, *MNRAS*, 441, 3040
- Borkowski, K. J., Hendrick, S. P., & Reynolds, S. P. 2007, *ApJ*, 671, L45
- Cash, W. 1979, *ApJ*, 228, 939
- Castro, D., & Slane, P. 2010, *ApJ*, 717, 372
- Dickel, J. R., & Milne, D. K. 1995, *AJ*, 109, 200
- Dogiel, V., Chernyshov, D., Koyama, K., Nobukawa, M., & Cheng, K.-S. 2011, *PASJ*, 63, 535
- Ellison, D. C., Patnaude, D. J., Slane, P., & Raymond, J. 2010, *ApJ*, 712, 287
- The Fermi-LAT Collaboration 2015, arXiv:1509.06903
- Frail, D. A., Goss, W. M., Reynoso, E. M., et al. 1996, *AJ*, 111, 1651
- Gabici, S., Aharonian, F. A., & Casanova, S. 2009, *MNRAS*, 396, 1629
- Gabici, S., & Aharonian, F. A. 2014, *MNRAS*, 445, L70
- Giacani, E., Smith, M. J. S., Dubner, G., et al. 2009, *A&A*, 507, 841
- Harrison, F. A., Craig, W. W., Christensen, F. E., et al. 2013, *ApJ*, 770, 103
- Helder, E. A., & Vink, J. 2008, *ApJ*, 686, 1094-1102
- H.E.S.S. Collaboration, Abramowski, A., Aharonian, F., et al. 2015, *Science*, 347, 406
- H. E. S. S. Collaboration, Abdalla, H., et al. 2016, arXiv:1609.08671
- Hitomi Collaboration, Aharonian, F., Akamatsu, H., et al. 2017, *PASJ*, in press (arXiv:1712.02365)
- Hughes, J. P., Hayashi, I., & Koyama, K. 1998, *ApJ*, 505, 732
- Hwang, U., & Laming, J. M. 2012, *ApJ*, 746, 130
- Inoue, T., Yamazaki, R., Inutsuka, S.-i., & Fukui, Y. 2012, *ApJ*, 744, 71
- Kalberla, P. M. W., Burton, W. B., Hartmann, D., et al. 2005, *A&A*, 440, 775
- Koyama, K., Petre, R., Gotthelf, E. V., et al. 1995, *Nature*, 378, 255
- Koyama, K., Tsunemi, H., Dotani, T., et al. 2007, *PASJ*, 59, 23
- Krimm, H. A., Holland, S. T., Corbet, R. H. D., et al. 2013, *ApJS*, 209, 14
- Liu, Q. Z., van Paradijs, J., & van den Heuvel, E. P. J. 2005, *A&A*, 442, 1135
- Macri, L. M., Stanek, K. Z., Bersier, D., Greenhill, L. J., & Reid, M. J. 2006, *ApJ*, 652, 1133
- Mitsuda, K., Bautz, M., Inoue, H., et al. 2007, *PASJ*, 59, 1
- Matsumoto, H., Ueno, M., Bamba, A., et al. 2007, *PASJ*, 59, 199
- Morse, J. A., Winkler, P. F., & Kirshner, R. P. 1995, *AJ*, 109, 2104
- Nakajima, H., Yamaguchi, H., Matsumoto, H., et al. 2008, *PASJ*, 60, 1
- Nakamura, R., Bamba, A., Dotani, T., et al. 2012, *ApJ*, 746, 134
- Nobukawa, K. K., Nobukawa, M., Uchiyama, H., et al. 2015, *ApJ*, 807, L10
- Ohira, Y., Murase, K., & Yamazaki, R. 2010, *A&A*, 513, A17
- Ohira, Y., Murase, K., & Yamazaki, R. 2011, *MNRAS*, 410, 1577
- Ohira, Y., Yamazaki, R., Kawanaka, N., & Ioka, K. 2012, *MNRAS*, 427, 91
- Ohira, Y., & Yamazaki, R. 2017, *Journal of High Energy Astrophysics*, 13, 17
- Ozawa, M., Koyama, K., Yamaguchi, H., Masai, K., & Tamagawa, T. 2009, *ApJ*, 706, L71
- Palmer, D. M., Grupe, D., & Krimm, H. A. 2007, *The Astronomer's Telegram*, 1169,
- Planck Collaboration, Ade, P. A. R., Aghanim, N., et al. 2014, *A&A*, 571, A28
- Plucinsky, P., Foster, A., Gaetz, T., et al. 2015, *Exploring the Hot and Energetic Universe: The first scientific conference dedicated to the Athena X-ray observatory*, 65
- Points, S. D., Chu, Y.-H., Snowden, S. L., & Smith, R. C. 2001, *ApJS*, 136, 99
- Ptuskun, V. S., & Zirakashvili, V. N. 2005, *A&A*, 429, 755
- Reynolds, S. P., & Moffett, D. A. 1993, *AJ*, 105, 2226
- Rho, J., & Petre, R. 1998, *ApJ*, 503, L167
- Russell, S. C., & Dopita, M. A. 1992, *ApJ*, 384, 508
- Sano, H., Fukui, Y., Yoshiike, S., et al. 2015, *Revolution in Astronomy with ALMA: The Third Year*, 499, 257
- Sato, T., Koyama, K., Takahashi, T., Odaka, H., & Nakashima, S. 2014, *PASJ*, 66, 124
- Sato, T., Koyama, K., Lee, S.-H., & Takahashi, T. 2016a, *PASJ*, 68, S8
- Sato, T. 2016b, Ph.D. thesis, U. of Tokyo, Japan
- Sekiya, N., Yamasaki, N. Y., & Mitsuda, K. 2016, *PASJ*, 68, S31
- Serlemitsos, P. J., Soong, Y., Chan, K.-W., et al. 2007, *PASJ*, 59, 9
- Slane, P., Bykov, A., Ellison, D. C., Dubner, G., & Castro, D. 2016, *Multi-scale Structure Formation and Dynamics in Cosmic Plasmas*, 187
- Sollerman, J., Ghavamian, P., Lundqvist, P., & Smith, R. C. 2003, *A&A*, 407, 249
- Sutherland, R. S., & Dopita, M. A. 1995, *ApJ*, 439, 365
- Takahashi, T., Abe, K., Endo, M., et al. 2007, *PASJ*, 59, 35
- Tawa, N., Hayashida, K., Nagai, M., et al. 2008, *PASJ*, 60, S11
- Uchiyama, Y., Aharonian, F. A., Tanaka, T., Takahashi, T., & Maeda, Y. 2007, *Nature*, 449, 576
- Uchiyama, H., Ozawa, M., Matsumoto, H., et al. 2009, *PASJ*, 61, 9
- Uchiyama, Y., Maeda, Y., Ebara, M., et al. 2008, *PASJ*, 60, S35
- Ueda, Y., Takahashi, T., Inoue, H., et al. 1999, *ApJ*, 518, 656
- Ueno, M., Sato, R., Kataoka, J., et al. 2007, *PASJ*, 59, 171
- Valinia, A., Tatischeff, V., Arnaud, K., Ebisawa, K., & Ramaty, R. 2000, *ApJ*, 543, 733
- Vink, J., & Laming, J. M. 2003, *ApJ*, 584, 758
- Vogt, F., & Dopita, M. A. 2011, *Ap&SS*, 331, 521
- Williams, B. J., Borkowski, K. J., Reynolds, S. P., et al. 2006, *ApJ*, 652, L33
- Yamaguchi, H., Koyama, K., Nakajima, H., et al. 2008, *PASJ*, 60, S123
- Yamaguchi, H., Ozawa, M., Koyama, K., et al. 2009, *ApJ*, 705, L6
- Yamaguchi, H., Badenes, C., Petre, R., et al. 2014, *ApJ*, 785, L27
- Yamazaki, R., Kohri, K., Bamba, A., et al. 2006, *MNRAS*, 371, 1975
- Yamazaki, R., Kohri, K., & Katagiri, H. 2009, *A&A*, 495, 9
- Yoshino, T., Mitsuda, K., Yamasaki, N. Y., et al. 2009, *PASJ*, 61, 805

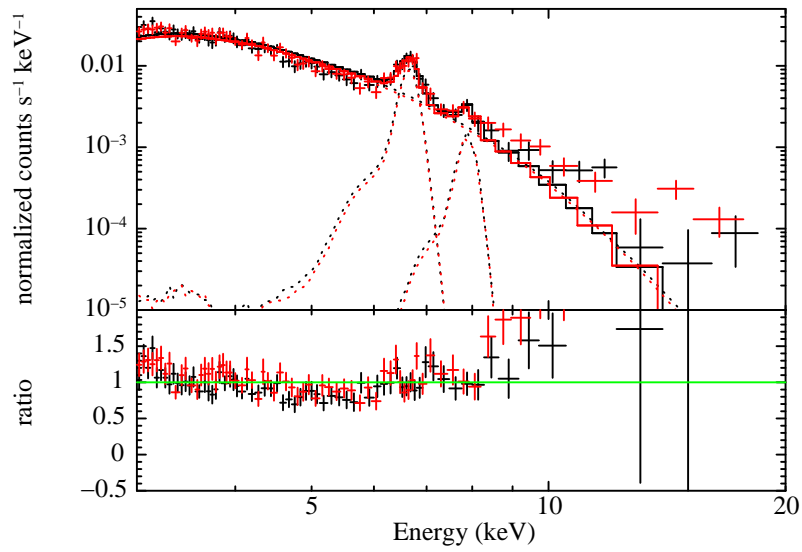


FIG. 2.— Background-subtracted *NuSTAR* spectra. Black and red crosses represent FPMA and FPMB data, respectively. Solid and dotted lines show the best-fit model of total and each component. The tails in the low energy side of lines are due to the detector response.

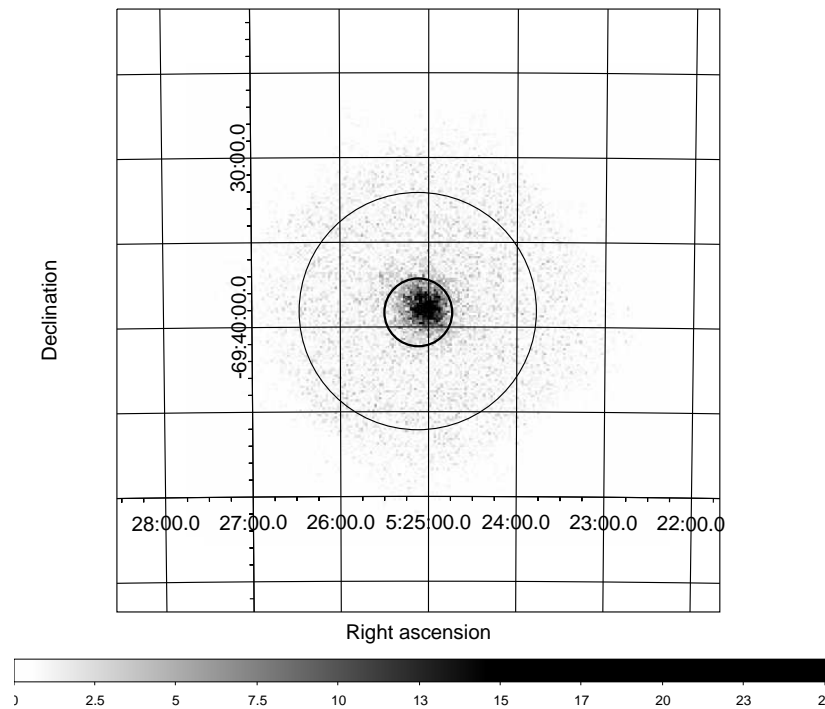


FIG. 3.— XIS3 image of N132D in the 5–10 keV band in J2000 coordinates. Neither vignetting correction nor NXB subtraction was performed. Thick and thin circles shows the region for the source and NXB estimation regions, respectively.

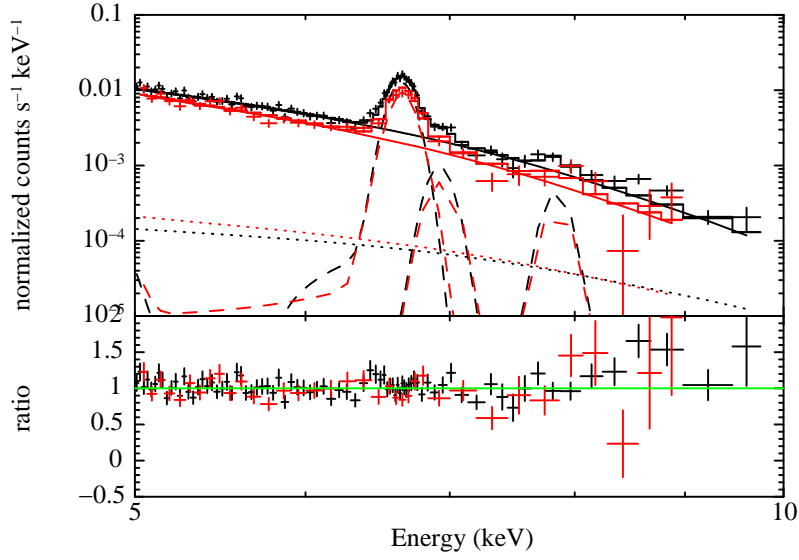


FIG. 4.— NXB-subtracted *Suzaku* XIS spectrum. Black and red crosses represent FI (XIS0+XIS3) and BI (XIS1) data. Solid, dashed, and dotted lines represent bremsstrahlung, gaussian components, and the CXB model, respectively. The tails in the low energy side of lines are due to the detector response.

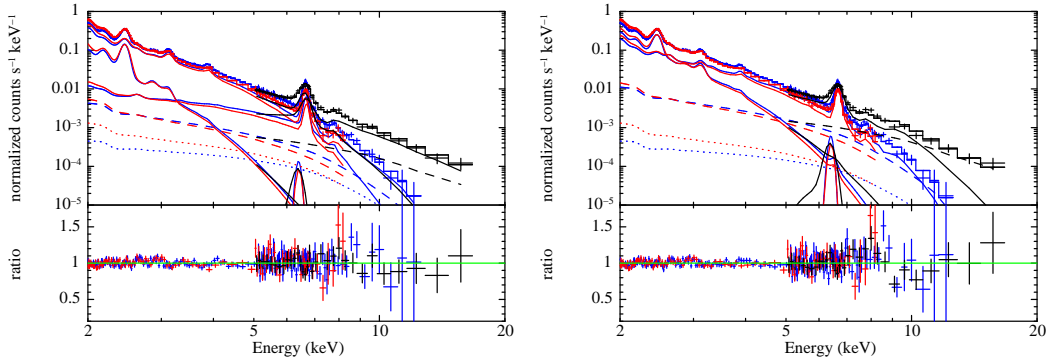


FIG. 5.— Wide-band spectral fitting result for model (a) (left) and model (b) (right) component models. Black, red, and blue crosses represent *NuSTAR*, *Suzaku* FI, and BI data set. Solid, dashed, and dotted lines represents thermal and power-law components, and the CXB for *Suzaku*.

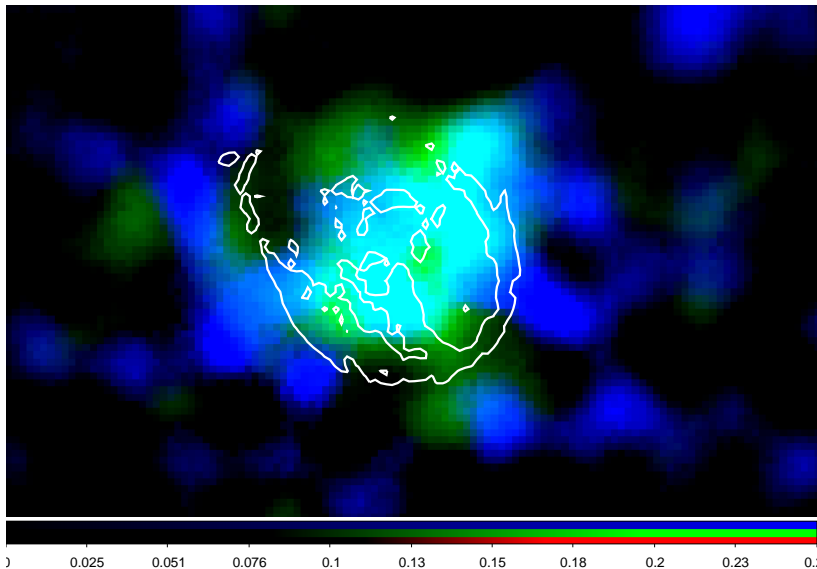


FIG. 6.— *NuSTAR* images of iron K line (blue) and 10–15 keV (green) bands in linear scale. Both images are smoothed with Gaussian model ($\sigma=9.8$ arcsec). White contour shows the *Chandra* image for the comparison.

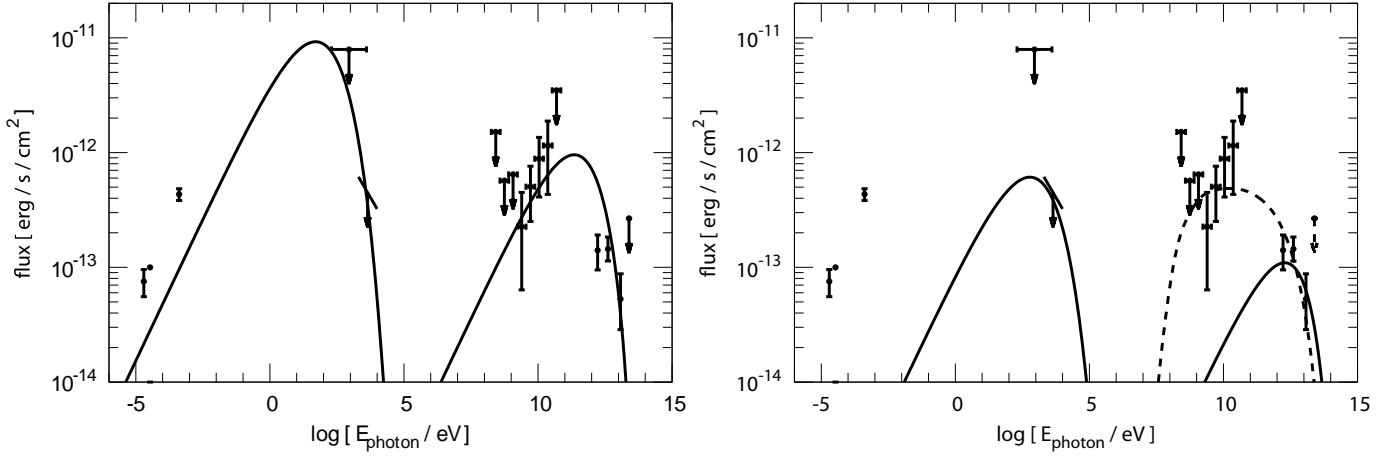


FIG. 7.— SED of N132D with pure leptonic (left) and leptonic + hadronic models (right), respectively (Dickel & Milne 1995; Planck Collaboration et al. 2014; Hughes et al. 1998; The Fermi-LAT Collaboration 2015; H.E.S.S. Collaboration et al. 2015). Solid and dashed lines represent leptonic and hadronic components, respectively. In the left panel, solid lines are for U_e of 2.5×10^{49} erg, cut-off energy of electrons of 7 TeV, and the magnetic field of $20 \mu\text{G}$, respectively. In the right panel, solid lines are for U_e of 10^{48} erg, the magnetic field of $13 \mu\text{G}$, and the maximum electron energy of 30 TeV, whereas dashed lines are for the maximum proton energy of 30 TeV, the total proton energy of 10^{50} erg, and the density of surrounding matter of 80 cm^{-3} . Although the pure leptonic model on the left shows good agreement with the data, it is physically unrealistic because it requires too much energy in the electrons.

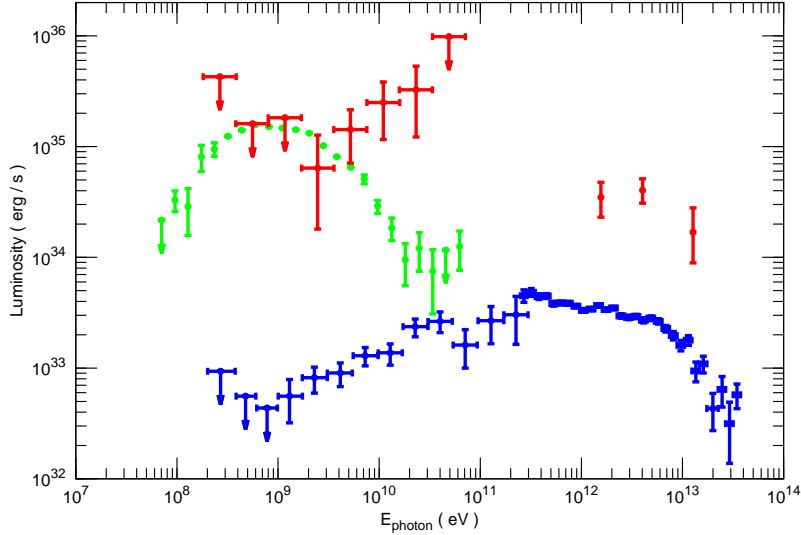


FIG. 8.— Gamma-ray spectra of young SNR sample (RX J1713–3946; blue), middle-aged sample (W44; green), and N132D (red). The horizontal axis represents $4\pi d^2 \times \nu F_\nu$, where d , ν , and F_ν are distance, frequency, and differential flux.

TABLE 1
OBSERVATION LOG

Satellite	ObsID	Date (YYYY/MM/DD)	Position (Ra, Dec.)	Exposure (ks)
<i>NuSTAR</i>	4010101000	2015/12/10	(81.3115, -69.6662)	62.3
<i>Suzaku</i>	105011010	2010/07/27	(81.2790, -69.6505)	35.8
<i>Suzaku</i>	106010010	2011/04/25	(81.2700, -69.6453)	26.0
<i>Suzaku</i>	106010020	2011/10/07	(81.2448, -69.6458)	23.9
<i>Suzaku</i>	107008010	2012/10/19	(81.2348, -69.6540)	24.1
<i>Suzaku</i>	107008020	2013/03/26	(81.2721, -69.6340)	23.1
<i>Suzaku</i>	108008020	2013/10/06	(81.2389, -69.6575)	5.1
<i>Suzaku</i>	108008030	2013/05/22	(81.2957, -69.6416)	29.8
<i>Suzaku</i>	108008040	2013/11/25	(81.2290, -69.6452)	27.1
<i>Suzaku</i>	108008050	2014/01/11	(81.2306, -69.6358)	7.5
<i>Suzaku</i>	109009010	2014/04/17	(81.2854, -69.6352)	24.9
<i>Suzaku</i>	109009020	2014/10/30	(81.2260, -69.6524)	13.5

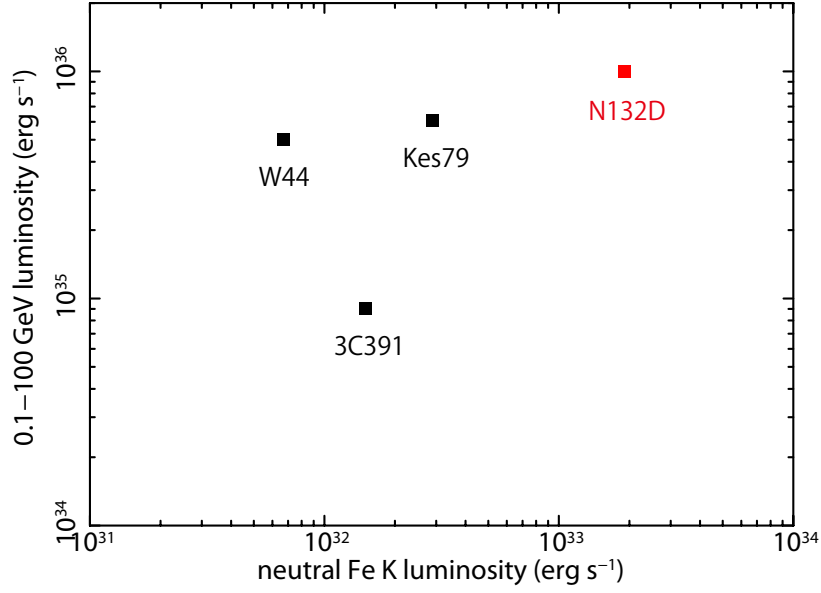


FIG. 9.— Relation between the neutral iron K line luminosity and 0.1–100 GeV gamma-ray luminosity. Red mark represents N132D (this work, The Fermi-LAT Collaboration 2015), whereas black ones are for Kes 79, W44, and 3C391 (Sato 2016b; Sato et al. 2016a; Auchettl et al. 2014; Acero et al. 2016).

TABLE 2
BEST-FIT PARAMETERS FOR THE NUSTAR
SPECTRA^a

Parameters	
Bremss	
kT (keV)	1.71 (1.65–1.78)
Norm ^b	7.6 (6.9–8.3)
Gaussian 1	
E_c (keV)	6.655 (6.641–6.677)
Flux ^c	13.4 (11.9–14.9)
Gaussian 2	
E_c (keV)	7.92 (7.81–7.98)
Flux ^c	2.3 (1.5–3.2)
cstat/d.o.f.	287.8/131

^aErrors indicate single parameter 90% confidence regions.

^bEmission measure in the unit of $\frac{3.02 \times 10^{-15}}{4\pi D^2} \int n_e n_i dV$, where D is the distance to the source (cm) and n_e , n_i are the electron and ion densities (cm^{-3}).

^cIn the unit of 10^{-6} photons $\text{cm}^{-2} \text{s}^{-1}$.

TABLE 3
BEST-FIT PARAMETERS FOR THE SUZAKU
SPECTRA^a

Parameters	
Bremss	
kT (keV)	2.25 (2.02–2.35)
Norm ^b	3.4 (3.0–4.3)
Gaussian 1	
E_c (keV)	6.652 (6.648–6.660)
Flux ^c	14.8 (14.0–15.5)
Gaussian 2	
E_c (keV)	6.92 (6.88–6.98)
Flux ^c	1.2 (0.8–1.7)
Gaussian 3	
E_c (keV)	7.85 (7.77–7.93)
Flux ^c	0.9 (0.5–1.4)
cstat/d.o.f.	145.4/109

^aErrors indicate single parameter 90% confidence regions.

^bEmission measure in the unit of $\frac{3.02 \times 10^{-15}}{4\pi D^2} \int n_e n_i dV$, where D is the distance to the source (cm) and n_e , n_i are the electron and ion densities (cm^{-3}).

^cIn the unit of 10^{-6} photons $\text{cm}^{-2}\text{s}^{-1}$.

TABLE 4
BEST-FIT PARAMETERS FOR THE COMBINED *Suzaku* AND *NuSTAR* SPECTRA^a

Parameters	model (a) ^b	model (b) ^b
low kT comp.		
kT (keV)	0.54 (0.39–0.56)	0.70 (0.65–0.71)
Z_{Si}	1.9 (>1.4)	0.63 (0.59–0.74)
Z_{S}	2.1 (>1.8)	0.91 (0.86–1.10)
Norm ^c	3.3 (0.1–4.1)	5.6 (4.7–5.8)
middle kT comp.		
kT (keV)	1.2 (0.8–1.2)	1.5 (1.3–1.6)
kT_{init} (keV)	—	> 8
$Z_{\text{Si}} = Z_{\text{S}}$	0.45 (0.40–0.48)	0.42 (0.36–0.49)
$Z_{\text{Fe}} = Z_{\text{Ni}}$	0.74 (0.61–0.96)	0.46 (0.40–0.57)
$n_e t$ (10^{11} s cm^{-3})	—	8.8 (7.0–10.0)
Norm ^c	2.8 (2.5–4.0)	1.3 (1.2–1.7)
high kT comp.		
kT (keV)	5.7 (4.0–6.8)	—
Norm ^c	0.06 (0.05–0.10)	—
Neutral iron line		
Flux ^d	1.5 (<5.7)	6.7 (2.0–11.0)
Power-law		
Γ	2.4 (fixed)	2.4 (fixed)
$F_{2-10\text{keV}}$ (10^{-13} erg $\text{cm}^{-2}\text{s}^{-1}$)	1.9 (0.5–4.1)	5.0 (4.2–7.3)
Gain fit for XIS FI (eV)	3.9	5.4
Gain fit for XIS BI (eV)	11.7	9.8
cstat/d.o.f.	419.5/323	431.3/323

^aErrors indicate single parameter 90% confidence regions.

^bModel (a) is 3 *vap*ec model, and Model (b) is 2 *apec* + *vrnei* + power-law model.

^cEmission measure in the unit of $\frac{10^{-16}}{4\pi D^2} \int n_e n_i dV$, where D is the distance to the source (cm) and n_e , n_i are the electron and ion densities (cm^{-3}).

^dIn the unit of 10^{-7} photons $\text{cm}^{-2}\text{s}^{-1}$.